Materials & Design 225 (2023) 111609

Contents lists available at ScienceDirect

Materials & Design

journal homepage: www.elsevier.com/locate/matdes

Microstructure characterisation of multi-principal element alloys welds produced by electron beam welding

Ricardo Henrique Buzolin [a,b,*], Tim Richter [c], Florian Pixner [b], Michael Rhode [c,d], Dirk Schroepfer [c], Norbert Enzinger [b]

[a] Christian Doppler Laboratory for Design of High-Performance Alloys by Thermomechanical Processing, Kopernikusgasse 24, 8010 Graz, Austria
[b] Institute of Materials Science, Joining and Forming at Graz, University of Technology, Kopernikusgasse 24/I, 8010 Graz, Austria
[c] Bundesanstalt für Materialforschung und -prüfung (BAM), Department 9. Component Safety, Berlin, Germany
[d] Otto-von-Guericke Universität, Institute for Materials Science and Joining Technology, Magdeburg, Germany

HIGHLIGHTS

- Twins are suppressed in the fusion zone.
- There is no indication of heat affected zone for the medium or high entropy alloy welds in the annealed condition.
- Finer elongated grains are formed in the fusion zone of the high entropy alloy than that of the medium entropy alloy.
- A specific ⟨100⟩ fibre along the transversal direction and specific texture components are formed in the fusion zone of the high entropy alloy and medium alloy welds, respectively.

GRAPHICAL ABSTRACT

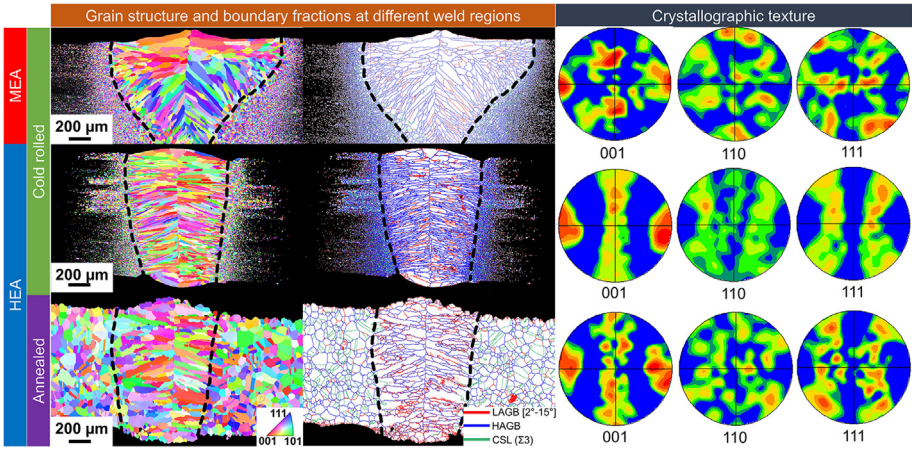

ARTICLE INFO

Article history:
Received 18 November 2022
Revised 31 December 2022
Accepted 6 January 2023
Available online 07 January 2023

Keywords:
Multi-principal element alloys
High entropy alloys (HEA)
Medium entropy alloys (MEA)
Electron beam welding (EBW)
Microstructure
Electron backscattered diffraction (EBSD)

ABSTRACT

This work explores the feasibility of producing bead-on-plate welds of a CrCoNi medium entropy alloy and a CrMnFeCoNi high entropy alloy using electron beam welding. The alloys were welded in two states: one in an as-cold-rolled condition and the other in an annealed condition. In addition, the materials are welded with two different parameters. The FCC microstructure of the welds is investigated using scanning electron microscopy assisted by energy-dispersive X-ray spectroscopy and electron-backscattered diffraction. The impact of the weld on the microstructure is discussed. The heat-affected zone is negligible for the annealed condition of both medium and high entropy alloys since there is no driving force for recrystallisation and the exposure time to high temperature is insufficient for grain coarsening. The texture formed in the fusion zone is also discussed and compared to the texture in the base metal and the heat-affected zone. Although the grain growth along the ⟨100⟩ crystallographic direction is preferential in all cases, the crystallographic texture type differs from each weld. Higher hardness values are measured in the medium entropy alloy's base metal and fusion zone than in the high entropy alloy.

* Corresponding author.
E-mail address: ricardo.buzolin@tugraz.at (R.H. Buzolin).

https://doi.org/10.1016/j.matdes.2023.111609
0264-1275/

1. Introduction

Multi-principal elemental alloys, also known as medium (MEA) and high entropy alloys (HEA), are a new class of material that received considerable attention in recent years [1–4]. They are alloys composed of three or more elements forming simple solid solution phases [5,6]. These alloys have been investigated due to their promising properties, either for structural applications, such as high fracture-resistant for cryogenic applications [7], high compressive strength [8], and a high strength-ductility ratio [9] or as functional materials, such as catalytical [10,11] or magnetic materials [12–14] and coatings for high-temperature or high oxidation resistance [15,16], among other fields.

Since, theoretically, infinite combinations of chemical elements and compositions can be used to produce a multi-principal elemental alloy, its development offers a great challenge to categorise the material behaviour according to its composition properly. Therefore, some works aimed to describe the alloys in terms of the crystal structure and present chemical elements [17], and others proposed to classify the alloys in terms of the operative strengthening mechanisms [2]. Among the several MEA and HEA, the ones containing 3d-transitional metallic elements with FCC crystal structure attracted attention due to their outstanding toughness and ductility, especially at low and even cryogenic temperatures [2,18]. Among those alloys, CrCoNi MEA [19] and a CrMnFeCoNi HEA [20] have been proposed and investigated in other works.

Whereas there is currently a certain basis for the effects of welding processes on multi-principal elemental alloys (mostly tungsten inert gas welding, friction stir welding, laser beam welding), this is still very limited for electron beam welding with a very few publications [21]. These are investigating on $Al_xCoCrFeNi$ alloys [22,23] and the most studied alloy with other welding processes, the single-phase CrMnFeCoNi HEA [24]. Nahmany et al. [22] show that during remelting with electron beam welding, distinct hot cracks form in the weld metal near the fusion line of an $Al_{0.8}CoCrFeNi$ alloy and a distinct hardening in the weld metal is observed. In contrast, this hardening does not occur to this extent in an $Al_{0.6}CoCrFeNi$ alloy, which also does not show any cracks. Sokkalingam et al. [23] investigated dissimilar metal electron beam welding of an $Al_{0.1}CoCrFeNi$ multi-principal elemental alloy with a conventional AISI 304 stainless steel. They showed good weldability without defects and a fully austenitic cellular dendritic microstructure. The influence of the welding on the microstructure (structure, grain size) in the heat-affected zone is also absent. The weldability of CrMnFeCoNi HEA was tested by Wu et al. [24] using thin plate welding tests. No solidification cracks were observed after welding. Furthermore, the welded materials maintained the strength and ductility of the base material at both room temperature and cryogenic temperatures, indicating good weldability of these HEAs in this condition. Nevertheless, the literature still raises questions concerning microstructure formation in electron beam welding. These include the characterisation of the heat-affected zone and a detailed description of the weld metal microstructure concerning the texture formation.

This work investigates the feasibility of producing defect-free bead-on-plate welds via electron beam welding of multi-principal alloys, particularly the ones based on 3d-transitional metallic elements with FCC crystal structure. A CrCoNi MEA and a CrMnFeCoNi HEA are used. Different welding parameters are used, and cold-rolled and annealed base metals are tested. The microstructure of the welds is investigated thoroughly, and the mechanisms responsible for the microstructure formation are discussed. This work aims to serve as a guideline for electron beam welding of multi-principal alloys, especially in describing the microstructure formation.

2. Experimental procedures

A CrCoNi MEA and a CrMnFeCoNi HEA were prepared by vacuum induction melting pure elements (purity: 99.9 wt%) and homogenisation at 1200 °C for 48 h afterwards. The material preparation is described in more detail in [25,26]. The ingots with a diameter of 40 mm were cold-rolled to sheets with a thickness of 1.2 mm. Some sheets were additionally recrystallised at 1020 °C (HEA) and 1060 °C (MEA) for 60 min. After that, a single-phase FCC alloy with some minor production-related impurities (Cr- and Mn-rich oxides) was present [27]. The chemical compositions of the alloys were determined by electron microprobe analysis (EMPA) and are listed in Table 1.

The welding tests were carried out with the electron beam welding (EBW) device pro-beam EBG 45–150 K14. The pressure in the working chamber with a nominal volume of about 1.4 m^3 was below $5x10^{-3}$ mbar. The beam axis of the EBW device is vertical, and all welds were performed in a flat position (PA, 1G). The focal position was set on the top surface of the plates and corresponded to a lens current of 2240 mA at a working distance of about 800 mm. The input parameters relevant to the process were determined based on a preliminary study and are listed in Table 2. Two different beam current levels, i.e. 8 and 9 mA, were used. The two welds of the HEA were investigated using scanning electron microscopy, while only the weld produced with beam current level of 8 mA was investigated using scanning electron microscopy for the MEA.

The cross-sections of the welds were cut, hot embedded and metallographically prepared using silicon carbide grinding papers up to grit 2000, followed by mechanical polishing using active oxide polishing suspension (OP-S). A Tescan Mira3 scanning electron microscopy (SEM) equipped with an energy-dispersive X-ray (EDX) spectrometer and a Hikari Plus electron backscatter diffraction (EBSD) camera was used to investigate the polished weld cross-sections. One or more EBSD maps of the cross-section were measured using a step size of 1.5 μm and merged using the software OIM DataAnalysis 8.6. Only one phase was found and indexed according to a general FCC crystal structure. The EBSD data was cleaned using grain dilation for a grain size of at least 5 pixels considering a transition angle between low to high-angle grain boundaries of 15°. The kernel average misorientation was obtained using the 1st nearest neighbour. The Σ3 boundaries were calculated using a tolerance of $15 \cdot (''\Sigma'')^{0.5}$. The texture was evaluated using the harmonic series expansion using no sample symmetry and using all measured points. The series rank of 16 and 5° of Gaussian Half-width were used for pole figure calculations.

Hardness measurements were performed in the polished weld cross-sections using an automated EMCO DuraScan 80 G5 according to the standard DIN EN ISO 6507–4: 2006–03. Vickers hardness (HV) was measured at a load of 0.1 kp and a dwell time of 15 s. The distance between adjacent indentations was 180 μm, and hardness

Table 1
Chemical composition (in atomic %) of CrMnFeCoNi HEA and CrCoNi MEA by EMPA.

	Co	Cr	Fe	Mn	Ni
HEA	19.7	20.7	19.6	20.1	19.9
MEA	33.0	34.3	–	–	32.7

Table 2
Summary of relevant input parameters for electron beam welding of MEA and HEA sheets in as-rolled and annealed conditions.

Attribute		Values	Unit
Acceleration Voltage	U_{acc}	80	kV
Beam Current	I_{beam}	8 / 9	mA
Welding Speed	v_{weld}	25	mm/s
Input Power	P	640 / 720	W
Input Energy	E	25.6 / 28.8	J/mm
Focal Position	f_p	Surface	–
Beam Figure	–	Circle	–
Oscillation Frequency	f	1000	Hz
Amplitude of Deflection	x,y	Ø 0.5	mm
Working Distance	–	800	mm

maps were derived from the measurements and visualised with MATLAB software.

3. Results and discussion

The microstructure of the produced bead-on-plate welds of the MEA and HEA are characterised using scanning electron microscopy (SEM) assisted by electron backscattered diffraction (EBSD) and energy-dispersive X-ray spectroscopy (EDX).

3.1. MEA

Both configurations, i.e., the as-rolled and the annealed condition, were welded with similar parameter settings. In general, full penetration was achieved at 9 mA, while critical penetration was achieved at 8 mA, as seen in Fig. 1. Considering the visual appearance of the 8 mA annealed and 9 mA as-rolled weld geometry, a transition from conduction to keyhole welding is observed. It is noted that there are also differences in weld geometry in the rolled and annealed samples in general. The weld geometry changes from a stemless wine glass shape to a nail head shape in the annealed to rolled condition (i.e., transition conduction welding to keyhole welding). A similar observation was made by Mei et al. [28], who found that the weld shape transforms from a stemless wine glass shape to a nail head shape with the increase of the grain size of base metal for similar parameter settings for different investigated initial microstructures of Inconel® 718.

The cross-section overview of the MEA with cold-rolled initial microstructure is shown in Fig. 2. Only FCC phase was detected in the EBSD measurement. The high dislocation and boundary densities in the cold-rolled base metal microstructure prevent resolving the sub and grain structures with EBSD. Fig. 2a shows the inverse pole figure map (IPF). It is possible to distinguish the base metal (BM), the heat-affected zone (HAZ) and the fusion zone (FZ). The weld centreline is clearly defined since the grains form a well-defined centreline between the "left" and "right" zones of the FZ. Columnar grains are formed in the FZ. Fig. 2b shows the boundary map where the low-angle grain boundaries (LAGB), high-angle grain boundaries (HAGB), and coincidence site lattice (CSL) Σ3 boundaries are indicated in red, blue, and green lines, respectively. A gradient of boundary distribution from the base metal towards the centre of the weld is visible. The grain size at the fusion boundary is dictated by the epitaxial growth of the HAZ grains, and the grain size/width increases as grain growth proceed to the weld centerline. The BM's highly deformed and unresolved microstructure progressively recovers and recrystallises at the HAZ as a function of the reached peak temperature during welding. The columnar grains in the FZ are mainly formed by LAGB and HAGB, while some CSL Σ3 boundaries are visible in the HAZ. Fig. 2c shows the kernel average misorientation (KAM) map of the MEA with cold-rolled initial microstructure. The LAGB present in the FZ has small values of KAM, visible as the green lines or regions in the FZ. A gradient in KAM is present in the HAZ. The stored energy due to cold-rolling, also seen as high KAM values, drives the HAZ's static recrystallisation and recovery. There is no evidence of abnormal grain growth in the HAZ as relatively homogeneous grain size is observed as a function of the distance from the HAZ and base metal (BM) interface, dedicated to the nature of the process and rapid welding speeds combined with a high-density heat source. Similar observations are also made for EBW of SPD material in processed and annealed conditions [29]. The width of the HAZ is ∼ 500 μm on the top region of the weld and ∼ 1000 μm on the bottom region of the weld, considering the BM as the nearly unindexed material.

The HAZ in transformable steels is typically subdivided into several zones associated with the phase transformations that occur and the impact of temperature on the ferrite size and morphology [30]. Here, both alloys are single-phase and do not suffer allotropic transformations or precipitation. Thus, the HAZ of the investigated welds needs to be interpreted as the region that suffers microstructural changes differentiating it from the BM. Fig. 3 shows the detailed views of the microstructures of the HAZ (Fig. 3(a,c,e)) and FZ (Fig. 3(b,d,f)). The dashed lines in Fig. 3(a,c) indicate the

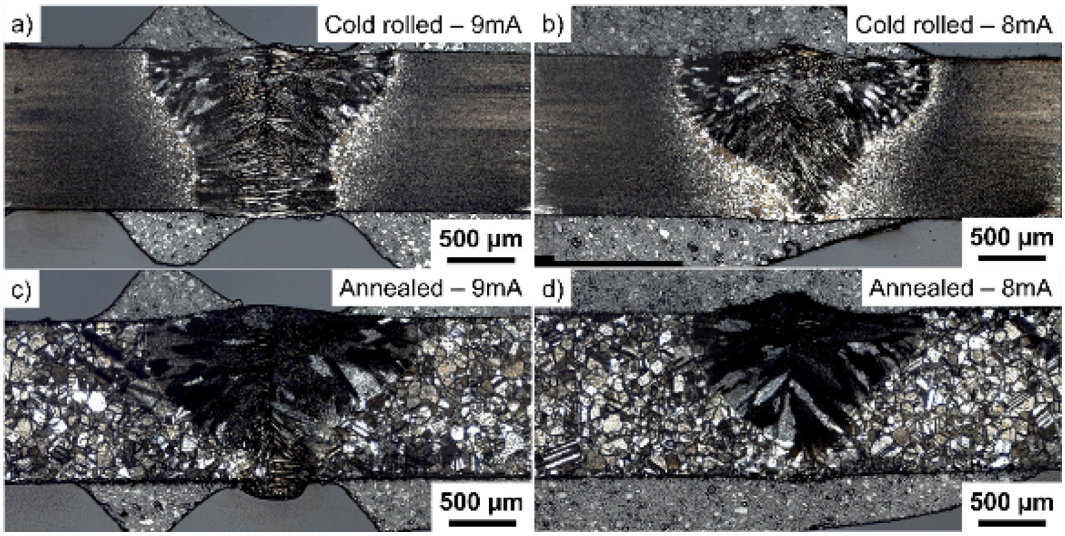

Fig. 1. Light micrographs of the cross-section of the MEA welded in the: a,b) cold-rolled state; c,d) annealed condition, and a,c) 9 mA; b,d) 8 mA.

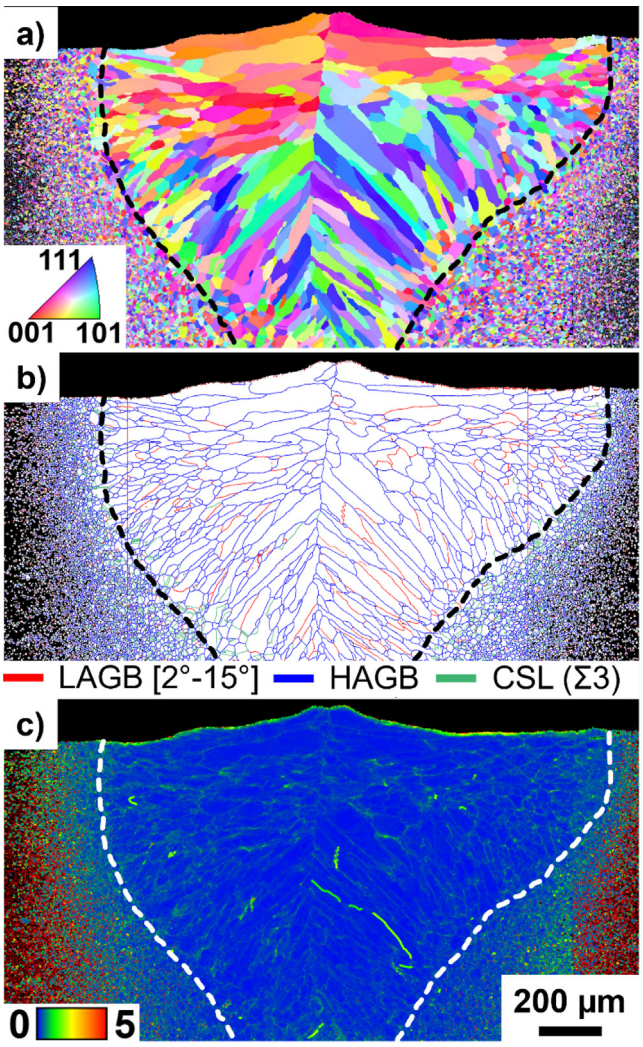

Fig. 2. Electron backscattered diffraction (EBSD) maps of the cross-section of the MEA welded in the cold-rolled state: a) inverse pole figure map; b) boundary map indicating the low angle grain boundaries (LAGB) in red, the high angle grain boundaries (HAGB) in blue and the coincidence site lattice (CSL) Σ3 boundaries in green; c) kernel average misorientation (KAM) map; dashed line represents the transition heat-affected zone to the fusion zone, namely fusion line.

position of the interface between HAZ and FZ, defined by the epitaxial grain growth from the coarsened grains in the HAZ along the direction opposite of the maximum heat flux. Fig. 3(e and f) shows the pole figures corresponding to the HAZ and FZ, respectively. While a {123} < $63\bar{4}$ > S-type texture is shown in HAZ, Fig. 3e, a {110} ⟨001⟩ Goss-type texture type is formed in the FZ, Fig. 3f. The S-type texture is typically known as the rolling texture for FCC metals, while the Goss texture is the usual recrystallisation texture in FCC metals [31,32]. Most HAZ is formed by small recrystallised grains, Fig. 3(a,c). Large recrystallised grains are mainly seen at the interface with the FZ. Fig. 3a shows elongated grains in the FZ that grow from the recrystallised ones at the HAZ. It shows that the fine recrystallised grains formed at lower temperatures in the HAZ preserved the S-type texture. The presence of Goss texture in the FZ can be explained either by I and/or II:

I. The large recrystallised grains of the FCC phase formed in the vicinity of the FZ had a Goss texture, which was kept by the competitive epitaxial growth in the melt pool during solidification driven by the temperature gradient towards the centreline that formed the elongated grains in the FZ.

II. The Goss texture is preferential for solidifying the FCC phase of the investigated MEA under boundary conditions during electron beam welding.

The initial solidification occurs as an FCC phase due to epitaxial growth at the partially melted FCC grains in the HAZ in contact with the liquid. The direction of the maximum temperature gradient towards the solid–liquid interface dictates the grain growth of the epitaxially oriented grains. The preferred crystallographic growth direction (⟨100⟩ for cubic materials) also influences grain growth. Thus, the initial grain growth of partially melted grains in the HAZ is followed by a competitive grain growth process during welding. The most favourably oriented grains grow faster than the less favourably oriented grains. The boundary of the elliptical weld pool is curved, producing a continuous change in the maximum temperature gradient direction from the fusion line to the weld centre. Thus, a given grain can be favourably orientated in a particular period but not during the entire solidification process. Consequently, a continual appearance of new grains toward the centreline is observed. A low to moderate growth rate during solidification is expected, considering the fast solidification rates achieved in EBW [33,34].

Fig. 3(c,d) shows that twins are rarely present in the FZ. At the same time, they are visible in the HAZ, indicating that CSL Σ3 boundaries are formed during recrystallisation but not during solidification. In addition, there is no evidence of abnormal grain growth in the HAZ. The diameter of the equiaxed grains in the HAZ is in the range of the minor axis of the columnar grains in the FZ. Thus, there is a progressive transition from full static recrystallised material in the vicinity of the FZ towards a finer microstructure and lower recrystallisation grade towards the BM.

Fig. 4(a,c) shows the cross-section of the EBW weld for the MEA with the initial annealed microstructure. Only FCC phase was detected in the EBSD measurement. The black dashed line indicates the interface between BM and FZ. The BM has negligible stored energy after annealing since a fully recrystallised microstructure is formed, as shown in Fig. 4(b,e). Consequently, nucleation of new grains does not occur in the HAZ. The grain size is already large and the total time exposed to high temperatures is insufficient for grain coarsening or visible modifications of the grain structure. Similarities can be observed for EB welded annealed FCC AA1050 aluminium alloy [29]. Thus, there is no evidence that the heat cycle during welding significantly modified the microstructure of the BM, and a HAZ cannot be identified in this condition.

Similarly to the weld of the MEA using the initial as-rolled microstructure shown in Fig. 3, the solidified grains are formed by competitive epitaxial growth driven by the temperature gradient towards the top of weld centreline, which is also visible in Fig. 4(a,c). The shape of the columnar grains in the FZ slightly differs between the MEA welded by EBW for the initial as-rolled and annealed microstructures, Fig. 3 and Fig. 4, respectively. The boundary density consists on the total length of boundaries divided by the measurement area. It is 63.1 mm^{-1} and 53.5 mm^{-1} in the FZ of the as-rolled and annealed MEA weld, respectively. Specifically, the density of high-angle grain boundaries is 52.2 mm^{-1} and 43.5 m^{-1} in the FZ of the as-rolled and annealed MEA weld, respectively. Thus, slightly smaller columnar grains are formed in the FZ of the as-rolled MEA compared to FZ formed in the annealed MEA weld, similar to the findings observed for an AA1050 [29]. The grains solidify epitaxially from larger ones in the BM of the annealed MEA compared to the smaller recrystallised grains in the HAZ of the as-rolled MEA. Consequently, slightly larger grains are formed in the FZ of the annealed than in the as-rolled MEA. In addition, a slightly more irregular shape of

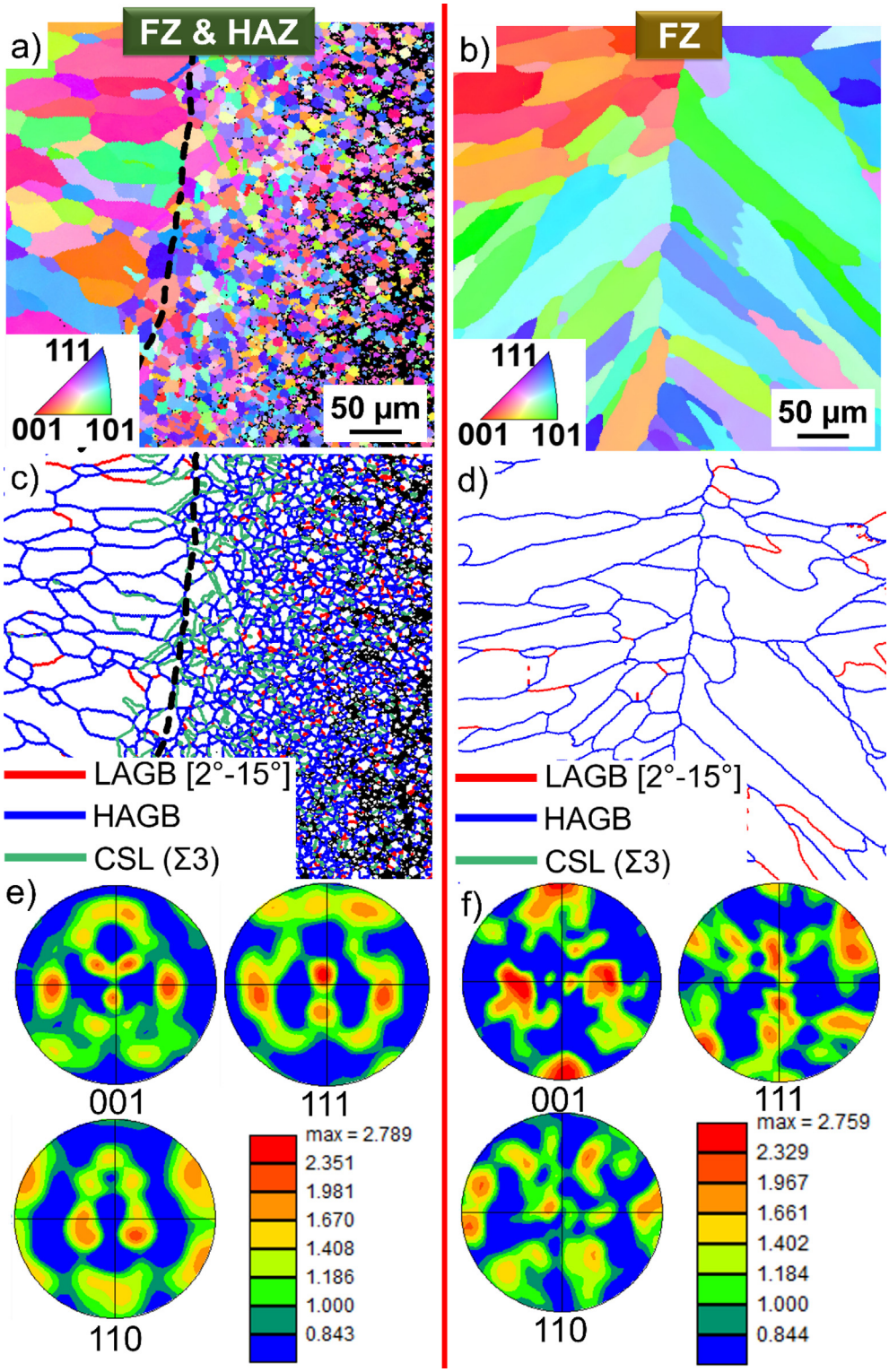

Fig. 3. Electron backscattered diffraction (EBSD) maps of the region comprising the heat-affected zone (HAZ) and fusion zone (FZ) of the MEA welded in the cold-rolled state: a,b) inverse pole figure maps of FZ and HAZ, and only FZ, respectively; c,d) boundary map of FZ and HAZ, and only FZ, respectively, indicating the low angle grain boundaries (LAGB) in red, the high angle grain boundaries (HAGB) in blue and the coincidence site lattice (CSL) Σ3 boundaries in green; e,f) pole figures of the HAZ and FZ, respectively. The dashed line represents the transition HAZ to the FZ, namely the fusion line.

the columnar grains in the FZ of the annealed MEA weld is observed compared to the FZ of the as-rolled MEA weld.

Fig. 4(e,f) shows the pole figures measured for the FZ and BM, respectively, of the annealed MEA. The BM has a mixed texture of weak and diffuse S ($\{123\}<63\bar{4}>$) and Brass ($\{110\}<1\,\bar{1}\,2>$) components, Fig. 4f. The FZ shows components for the S, Brass and, to a certain extent, the Goss texture, although the statistical relevance of the obtained data is limited as only a few grains are measured. The FZ of the annealed MEA seems to inherit more of

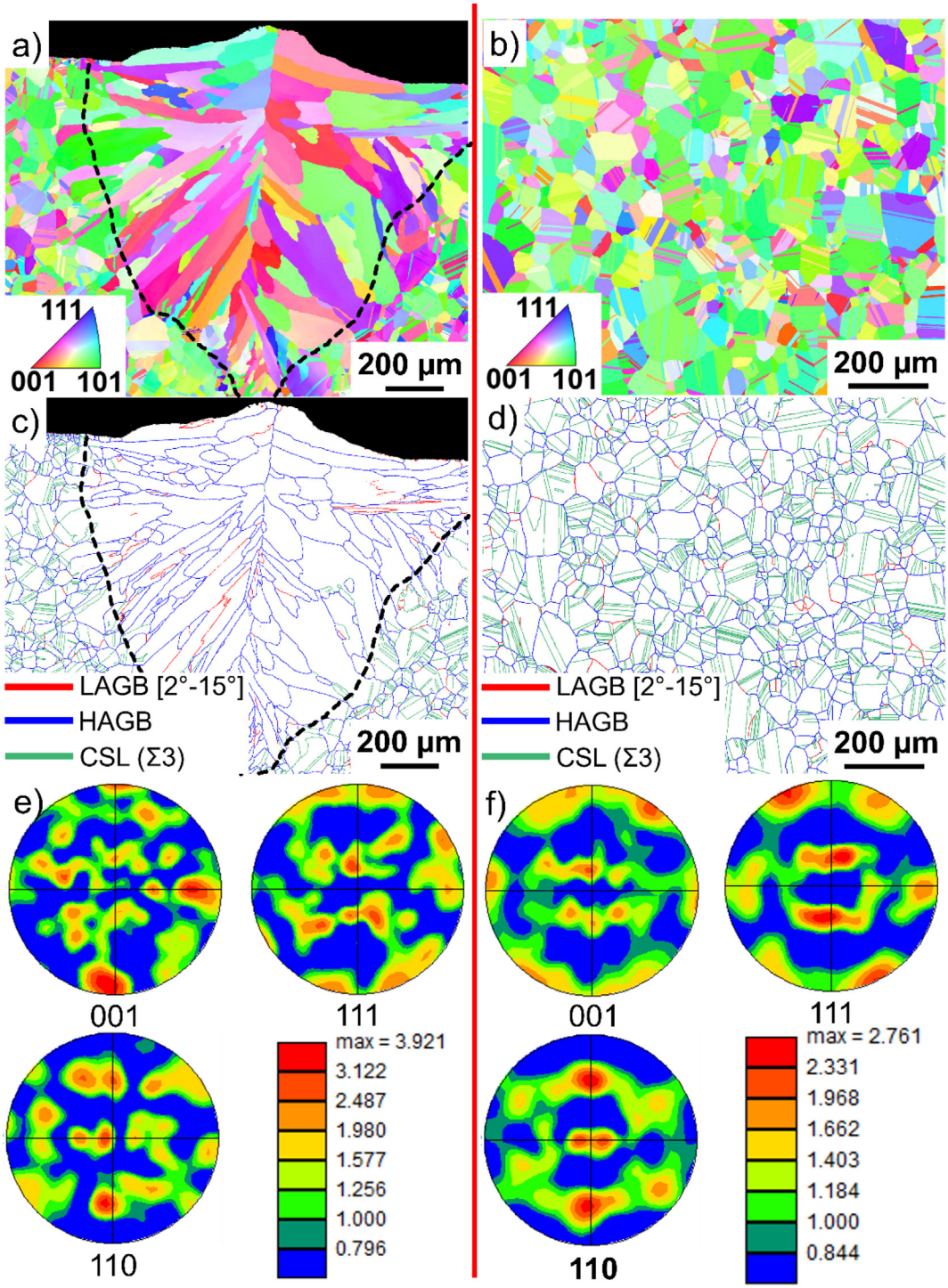

Fig. 4. Electron backscattered diffraction (EBSD) maps of the MEA in the annealed state: a,b) inverse pole figure maps of weld cross-section and base metal, respectively; c,d) boundary map of weld cross-section and base metal, respectively, indicating the low angle grain boundaries (LAGB) in red, the high angle grain boundaries (HAGB) in blue and the coincidence site lattice (CSL) Σ3 boundaries in green; e,f) pole figures of fusion zone and base metal, respectively. The black lines in a) and c) represent the transition from the base metal to the fusion zone, namely the fusion line. A heat-affected zone cannot be identified in the weld.

the crystallographic texture of the BM and HAZ than the as-rolled MEA.

3.2. HEA

To investigate the role of the heat input on the formed microstructure, the cross-sections of the HEA welded by EBW using two different beam energies, 8 mA and 9 mA, are shown in Fig. 5. Only FCC phase was detected in the EBSD measurements. The BM was cold-rolled and consequently had a fine microstructure with a high density of lattice defects. Therefore, they are seen as unindexed areas in Fig. 5. Full weld penetration is achieved in both cases, and a centreline is also visible. The dashed black lines indicate the interface between FZ and HAZ. Similar to the MEA, the initial solidification occurs as an FCC phase due to epitaxial growth at the partially melted FCC grains in the HAZ in contact

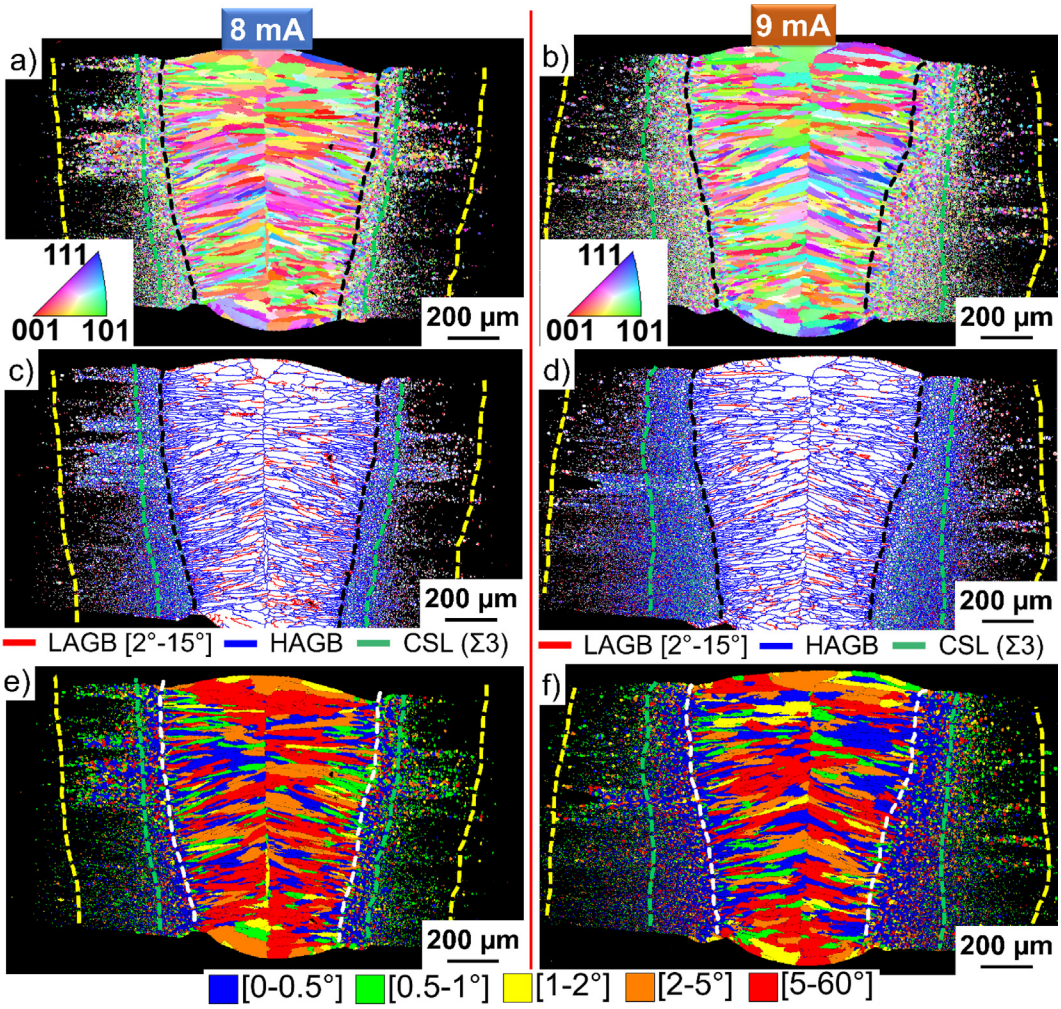

Fig. 5. Electron backscattered diffraction (EBSD) maps of the cross-section of the HEA electron beam welded in the cold-rolled state at: a,b) inverse pole figure map for 8 mA and 9 mA welding, respectively; c,d) boundary map for 8 mA and 9 mA welding, respectively, indicating the low angle grain boundaries (LAGB) in red, the high angle grain boundaries (HAGB) in blue and the coincidence site lattice (CSL) Σ3 boundaries in green; e,f) grain orientation spread (GOS) maps for 8 mA and 9 mA welding, respectively. The black and white dashed lines represent the transition heat-affected zone to the fusion zone, namely the fusion line, in (a-d) and (e,f), respectively. The green dashed lines illustrate a transition from an intensely recrystallised heat-affected zone to a partially recrystallised one. The yellow dashed lines illustrate a transition from a partially recrystallised heat-affected zone to the base metal.

with the liquid in the HEA welds. The microstructure is finer in the FZ of the HEA than in the MEA. Fig. 5(c,d) shows the boundary maps and the boundary density is notably larger in the HAZ compared to the FZ. The boundary density is high in the FZ in the vicinity of the HAZ and decreases towards the centreline.

Recrystallised grains form the HAZ and they are not homogeneously distributed from the FZ interface towards the BM. Considering a given distance from the FZ interface, regions with pronounced recrystallisation are neighbours of regions with less or no recrystallised grains (i.e. BM). Thus, a less homogeneous HAZ is formed in the as-rolled HEA (Fig. 5) compared to the as-rolled MEA (Fig. 2). It is probably related to the different distributions of stored energy in the as-rolled HEA that led to different recrystallisation kinetics when exposed to heat during welding. The green dashed lines in Fig. 5 delineate the HAZ where recrystallised grains are formed within its whole extension. It is visible in the grain orientation spread (GOS) map in Fig. 5(e,f), which shows a high fraction of grains with GOS below 0.5. The yellow dashed lines in Fig. 5 delineate the region where recrystallised grains are still observed, although the HAZ is not homogeneous or continuous in this region. The size of the HAZ delineated by the green dashed lines is of ~ 85 µm and ~ 100 to 300 µm for the EBW at 8 mA and 9 mA, respectively. In addition, the size of the HAZ delineated by the yellow dashed lines is of ~ 350 µm and ~ 450 to 600 µm for the EBW at 8 mA and 9 mA, respectively. Thus, the heat input impacts the temperature cycle and, consequently, the recrystallisation kinetics and grade, forming the HAZ.

Fig. 6 shows the detailed view of the HAZ and its interface with the FZ for the 8 mA weld of the HEA. The grain size is small for the recrystallised HAZ, and the solidified ones epitaxially grow from the interface. The grain boundaries in the FZ of the cold-rolled HEA, Fig. 5, are more tortuous than those in the FZ of the cold-rolled MEA, Fig. 3. Fig. 6(c and d) show the pole figures of the HAZ and FZ of the as-rolled HEA, respectively. A weak Brass-type ($\{1\,1\,0\} < 1\ \bar{1}\ 2 >$) texture is observed in the HAZ. The crystallographic texture in the FZ differs from the MEA, where no texture fibres are observed. The grain growth during solidification along the ⟨100⟩ direction without a preferential crystallographic plane is responsible for ⟨100⟩ fibre along the transversal direction (TD) in the FZ of the HEA. The slightly higher texture index indicates a slightly higher anisotropy in the FZ of the HEA than the FZ of the MEA. Thus, the finer grain structure formed in the FZ of the HEA welds also have the ⟨100⟩ as the preferential direction for the MEA welds but no specific crystallographic plane for grain growth

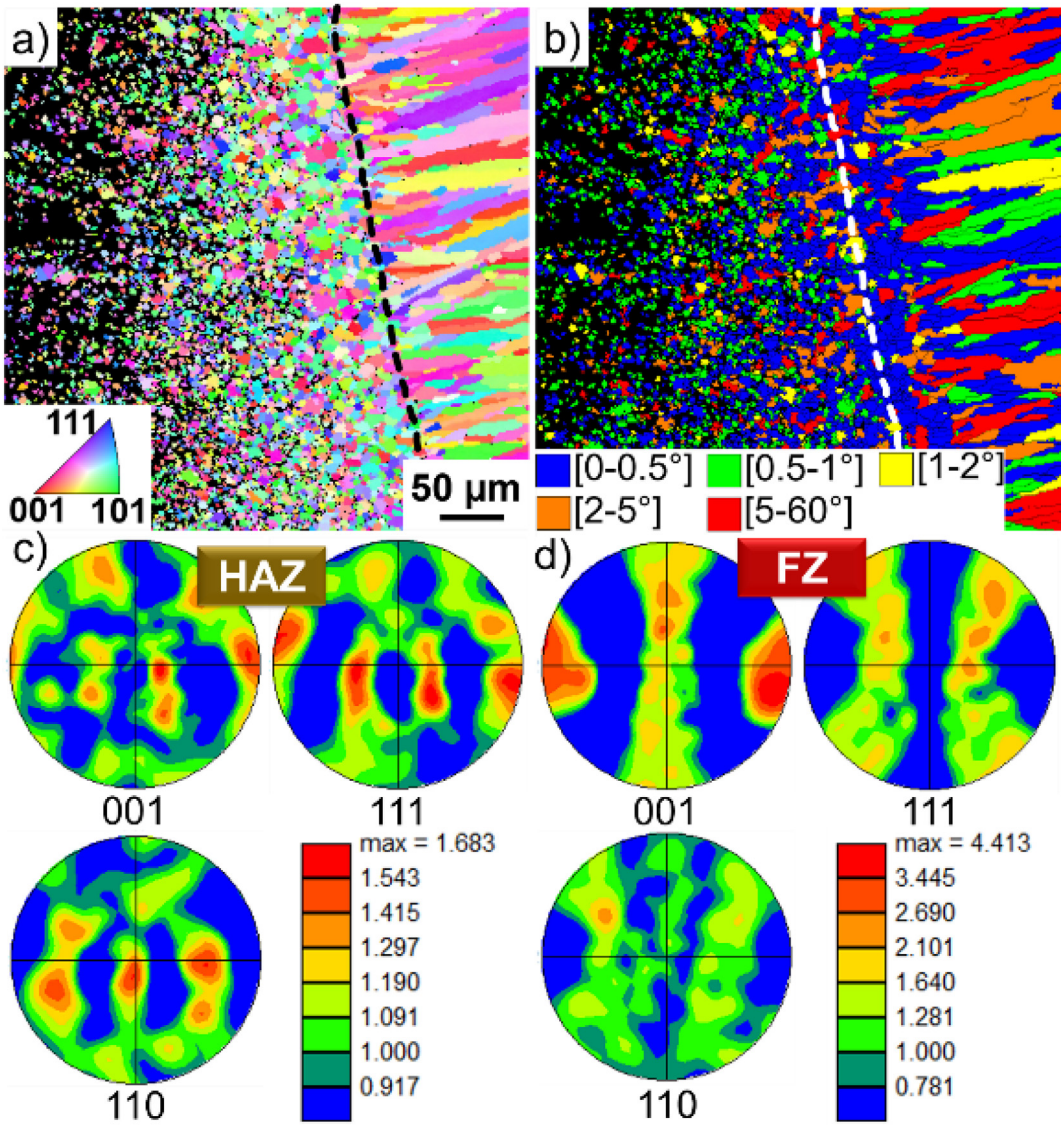

Fig. 6. Electron backscattered diffraction (EBSD) maps of the region comprising the heat-affected zone (HAZ) and fusion zone (FZ) of the HEA electron beam welded in the cold-rolled state at 8 mA: a) inverse pole figure map of FZ and HAZ; b) grain orientation spread (GOS) map of FZ and HAZ; c,d) pole figures of the HAZ and FZ, respectively. The black and white dashed lines in (a,b) represent the transition heat-affected zone to the fusion zone, namely the fusion line.

during solidification. Consequently, a fibre texture is formed in the FZ of the HEA welds instead of specific texture components observed in the MEA welds' FZ.

Fig. 7 shows the cross-sections of the EBW welds of the annealed HEA welded with 8 mA and 9 mA. Like the MEA (Fig. 4), the BM consists of a fully recrystallised microstructure, and a HAZ cannot be identified in the HEA welds of the annealed material. The grains are also columnar in the FZ of the annealed welded HEA (Fig. 7) but notably larger than those formed in the FZ of the as-rolled welded HEA (Fig. 6).

Fig. 8a shows a detailed view of the BM of the annealed HEA welded with 8 mA. The shape of the grains indicates their grain growth in the melt pool during solidification driven by the temperature gradient towards the centreline. There is a direct correlation between the grain size in the HAZ and the thickness of the columnar grains initially formed during solidification in the FZ for both the HEA and the MEA. The temperature gradient and the grain growth rate control the grain shape [35], but that is also a function of the chemical composition of the alloy. Considering the temperature gradients are comparable for the MEA and HEA since the heat input and plate thickness were similar, as well as the thermophysical properties (thermal conductivity [36], thermal expansion [37,38], it seems that the combination of finer grains at HAZ of the HEA and slower grain growth during solidification in the HEA produced a finer grain structure in the FZ of the HEA welds.

Fig. 8(b and c) show the pole figures of the BM and FZ, respectively, for the annealed HEA. The texture can be approximated in the BM by a mix of Copper-type ($\{112\}\langle 111\rangle$) and Goss-type ($\{110\}\langle 001\rangle$). The main components are preserved and an incomplete $\langle 100\rangle$ fibre along the TD direction is formed in the FZ of the HEA welded in the annealed state.

Table 3 summarises the texture components found in each zone of the welds. The texture is generally not strong or fully defined (i.e., diffuse) concerning the typically listed components in Table 3. The Brass, Copper and S textures are associated with the deformation texture formed in FCC materials, while the Goss texture is associated with recrystallisation texture in FCC materials [31,32]. The presence of S and Brass components in the BM of the MEA probably indicates that the material tends to retain the formed texture partially during deformation even after annealing [39,40]. On

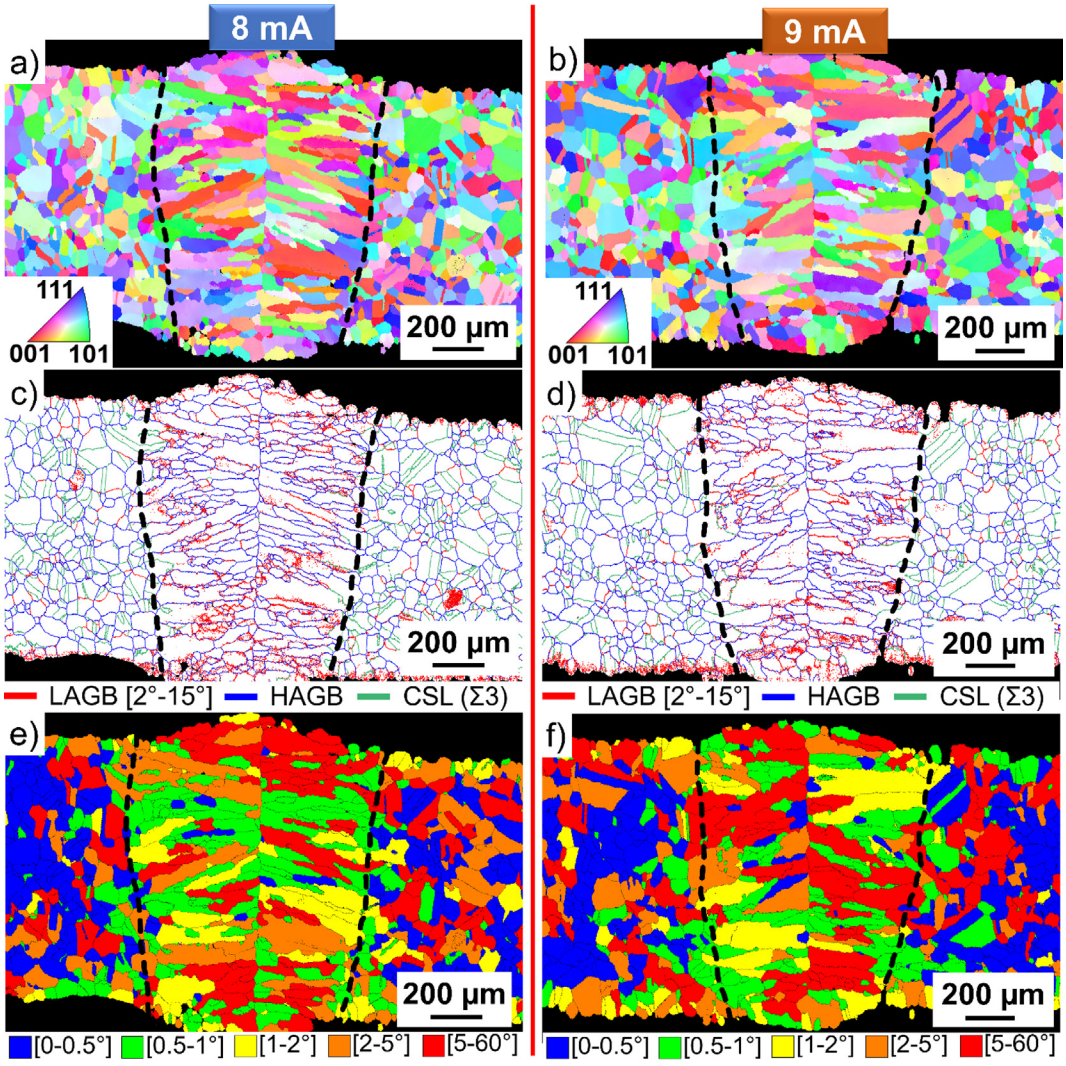

Fig. 7. Electron backscattered diffraction (EBSD) maps of the cross-section of the HEA electron beam welded in the annealed state at: a,b) inverse pole figure map for 8 mA and 9 mA welding, respectively; c,d) boundary map for 8 mA and 9 mA welding, respectively, indicating the low angle grain boundaries (LAGB) in red, the high angle grain boundaries (HAGB) in blue and the coincidence site lattice (CSL) Σ3 boundaries in green; e,f) grain orientation spread (GOS) maps for 8 mA and 9 mA welding, respectively. The black dashed lines represent the transition of the fusion zone to the base metal, namely the fusion line. No visible HAZ is present in the weld.

the other hand, the mixture of Copper and Goss components for the BM of HEA suggests a different deformation texture (Copper instead of S or Brass) compared to the MEA. The mixed texture character indicates that the deformation texture is partially kept after recrystallisation. The presence of S-type in the HAZ of the cold-rolled MEA corroborates the assumption that texture is kept after recrystallisation.

The Goss-type in the FZ of the MEA suggests that: I) either the grains in the vicinity to the FZ presented a Goss-type orientation; II) or the Goss-type is the favourable texture type for the columnar solidification for the investigated MEA. Regarding the cold-rolled HEA, the Brass texture in the HAZ corroborates the hypothesis that deformation texture can be retained after recrystallisation. In addition, the solidification forms a ⟨100⟩ fibre along the TD in the FZ of the HEA welds instead of specific components.

Fig. 9 shows the relative fraction of the CSL Σ3 boundary (twin boundary) to the fraction of HAGB for the BM of the annealed HEA as well as the FZ of the four welds of HEA. While a ratio higher than 0.5 is found for the BM, a value smaller than 0.05 is found in the FZ. The few twins are indicated in the black arrows in Fig. 9 for the annealed BM welded at 9 mA. Thus, in both MEA and HEA, the twins are formed due to recrystallisation but in a notably small amount during solidification, and in some cases, they are entirely suppressed.

3.3. Chemical composition analysis

Fig. 10 shows the chemical elemental maps obtained using energy-dispersive X-ray spectroscopy (EDX). The maps are measured in a region close to the centre of the weld. There is no evidence of macro-segregation or solute enrichment along the centreline of the weld. There is a slight solute segregation, especially of chromium. Cobalt enriches the dendrite core, while chromium enriches the interdendritic regions of the grains. Similar results were also found in a cast MEA of the same composition [41]. Despite minor solute segregation, there is no evidence of forming a BCC or Cr-rich sigma phase in the FZ. While the epitaxial nucleation at the fusion boundary controls the grain size formed in the FZ, the temperature gradient in the liquid at the solid–liquid interface and the solidification growth rate controls the elemental partitioning formed during solidification. Thus, the minor differences in the solidification cell sizes for the elemental partitions between annealed and cold-rolled, as seen in Fig. 10, indicate that

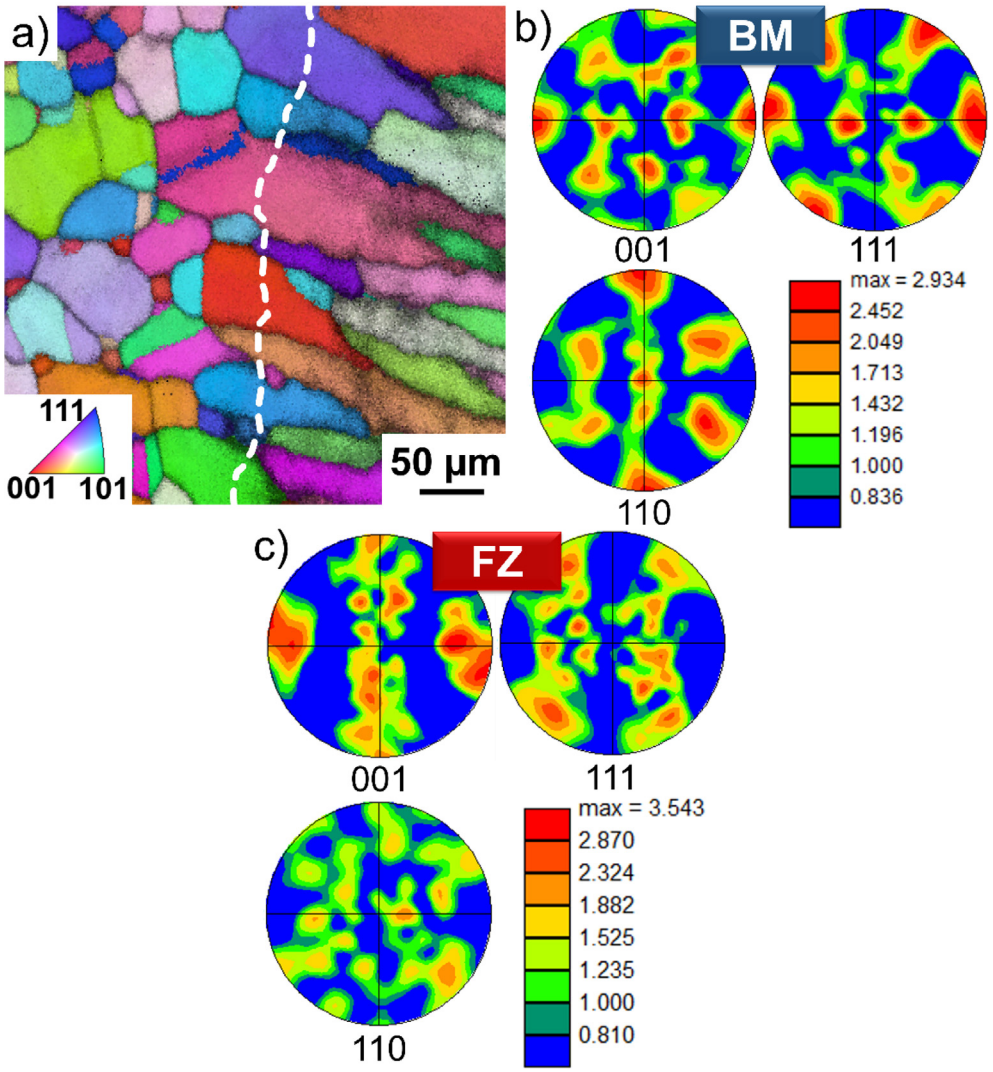

Fig. 8. Electron backscattered diffraction (EBSD) analysis of the HEA electron beam welded in the annealed state at 8 mA: a) inverse pole figure map of FZ; b,c) pole figures of the base metal (BM) and fusion zone (FZ), respectively. The white dashed lines in a) represent the transition from the FZ to the BM, namely the fusion line. A heat-affected zone cannot be identified in the weld.

Table 3
Summary of the observed texture fibre or components in the different regions of the produced welds. The specific component are: Brass: {1 1 0} < 1 $\bar{1}$ 2>; Copper: {1 1 2} ⟨1 1 1⟩; Goss: {1 1 0} ⟨0 0 1⟩; S: {1 2 3} < 6 3 $\bar{4}$>.

		BM	HAZ	FZ
MEA	Cold-rolled	–	S-type	Goss-type
	Annealed	A mix of weak S and Brass components	HAZ is negligible	A mix of S-type, Brass and, to a certain extent, the Goss components
HEA	Cold-rolled	–	Weak Brass-type	⟨1 0 0⟩ fibre along the TD
	Annealed	A mix of Copper-type and Goss-type	HAZ is negligible	Incomplete ⟨1 0 0⟩ fibre along the TD

the temperature gradient and the solidification growth rate were similar for the annealed and cold-rolled MEA welds.

Fig. 11 shows the EDX chemical elemental maps measured in the HEA welds' central region of the FZ. The sizes of the solidification cells seem to be slightly bigger in the 9 mA weld compared to the 8 mA attributed to the higher energy input for the 9 mA weld. Cobalt, chromium and iron enrich the dendrite core, while manganese and nickel enrich the interdendritic region of the grains, similar to the results obtained by Wu et al. [42]. A solidus of 1290 °C and a liquidus of 1340 °C were measured by Laurent-Brocq et al. [44], who also show that when the liquid phase is cooled down, the core dendrites is enriched in cobalt, chromium and iron. Afterwards, manganese and nickel enrich the interdendritic regions of the grain. The melting point of manganese and nickel are 1244 °C and 1453 °C respectively, while cobalt, chromium and iron have melting points of 1495 °C, 1857 °C and 1535 °C respectively. Thus, the elements with the lowest melting point enrich the interdendritic regions, in agreement with Cantor et al. [43] and Salishchev et al. [44]. Laurent-Brocq et al. [45] determined a partition coefficient of manganese and nickel in the chromium, iron and cobalt of 0.74 for a HEA of similar chemical composition investigated in this work.

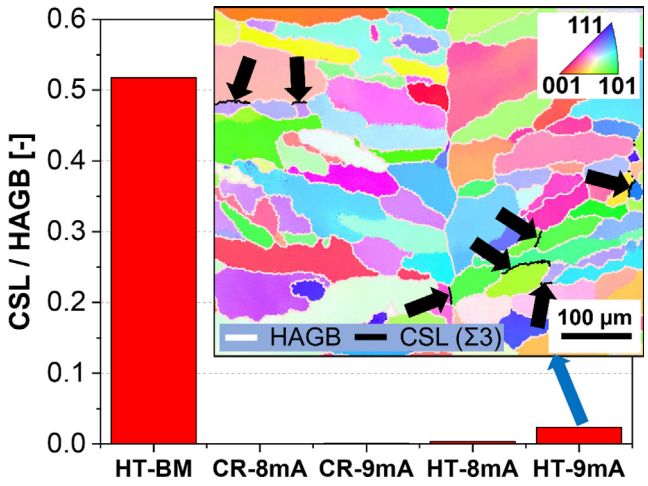

Fig. 9. The ratio between coincidence site lattice (CSL) Σ3 boundary density and high angle grain boundary (HAGB) density measured with electron backscattered diffraction (EBSD) for the HEA electron beam welded in the cold-rolled (CR) and annealed (HT) states at 8 mA and 9 mA. The base metal (BM) of the annealed HEA is considered. The black arrows in the inset indicate the CSL Σ3 boundaries.

3.4. Hardness

Fig. 12 shows the hardness maps for the MEA welds. The BM in the cold-rolled condition has a hardness of 482 ± 11 HV, while the annealed BM has 181 ± 8 HV. The difference in the hardness in the fusion zone between the different conditions is negligible and the mean value is approximately 195 HV, slightly higher than the annealed BM. A gradient in hardness is visible in the HAZ of the cold-rolled welds, Fig. 12(a,b). Slightly higher hardness values are observed in the BM near the FZ for the annealed BM, indicating a possible HAZ. However, the EBSD measurements do not indicate any visible microstructural change that can suggest the presence of a HAZ. Thus, the slightly higher hardness values in the BM near the FZ are probably related to residual stresses or microstructural modifications in the atomic scale that are undetectable with the EBSD technique for the performed measurements spatial resolution.

Fig. 13 shows the hardness maps for the HEA welds. The hardness values are smaller than in the MEA welds. The HEA BM in the cold-rolled condition has a hardness of 393 ± 8 HV, while the annealed HEA BM has 149 ± 6 HV. A mean value of approximately 178 HV is obtained for all FZs, slightly higher than the annealed BM. The harder zones in the FZ compared to the annealed BM can be explained by forming zones enriched with different chemical elements (microsegregation) and residual stresses. A similar gradient in hardness, as observed in the MEA welds, is also visible in the HAZ of the cold-rolled welds, Fig. 13 (a,b).

4. Summary and conclusions

Bead-on-plate welds of CrCoNi MEA and CrMnFeCoNi HEA are successfully produced using electron beam welding. The CrCoNi alloy is welded in the cold-rolled and annealed state. The CrMnFeCoNi alloy is welded with two different sets of parameters. No solidification of HAZ cracks was observed. The formed microstructure in the fusion zone (FZ), heat-affected zone (HAZ) and base metal (BM) are analysed thoroughly using scanning electron microscopy assisted by energy-dispersive X-ray spectroscopy and electron backscattered diffraction. The results allow drawing the following conclusions:

- Due to recrystallisation, CSL Σ3 twins are formed during annealing. They are present in a minor fraction in the FZ.
- The grains in the FZ initially nucleate epitaxially from the existing ones at HAZ/BM and grow during solidification driven by the temperature gradient towards the centreline solidification: the texture is partially kept, and grains are elongated and grow equally from both sides and meet quite accurately in the weld centre line.
- The HAZ of the welds for the cold-rolled condition can be defined as the region that suffers microstructural changes differentiating it from the BM. Since the material does not undergo phase transformation, the microstructural changes are associated with static recrystallisation and/or grain coarsening.
- Coarse and fine HAZs are not present in the case of an initial cold-rolled microstructure. The grain size progressively increases from the BM towards the FZ, and there is no evidence of abnormal grain growth.
- Static recrystallisation and/or grain coarsening does not occur in the region near the interface with the FZ for the initial annealed microstructure for both the MEA and HEA since there

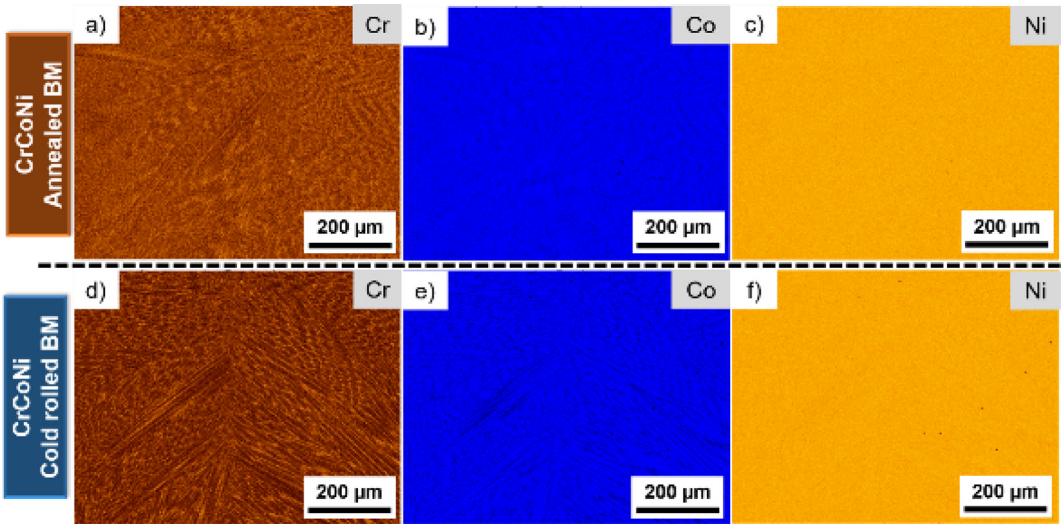

Fig. 10. Elemental map obtained from energy dispersive X-ray spectroscopy (EDX) for chromium, cobalt and nickel for the MEA electron beam welded in the cold-rolled and annealed states.

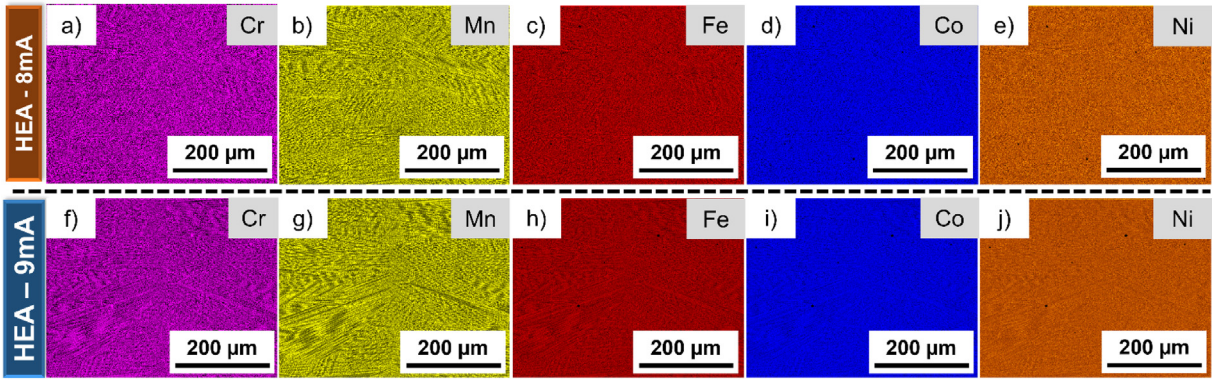

Fig. 11. Elemental map obtained from energy dispersive X-ray spectroscopy (EDX) for chromium, manganese, iron, cobalt and nickel for the HEA electron beam welded in the cold-rolled state at 8 mA and 9 mA.

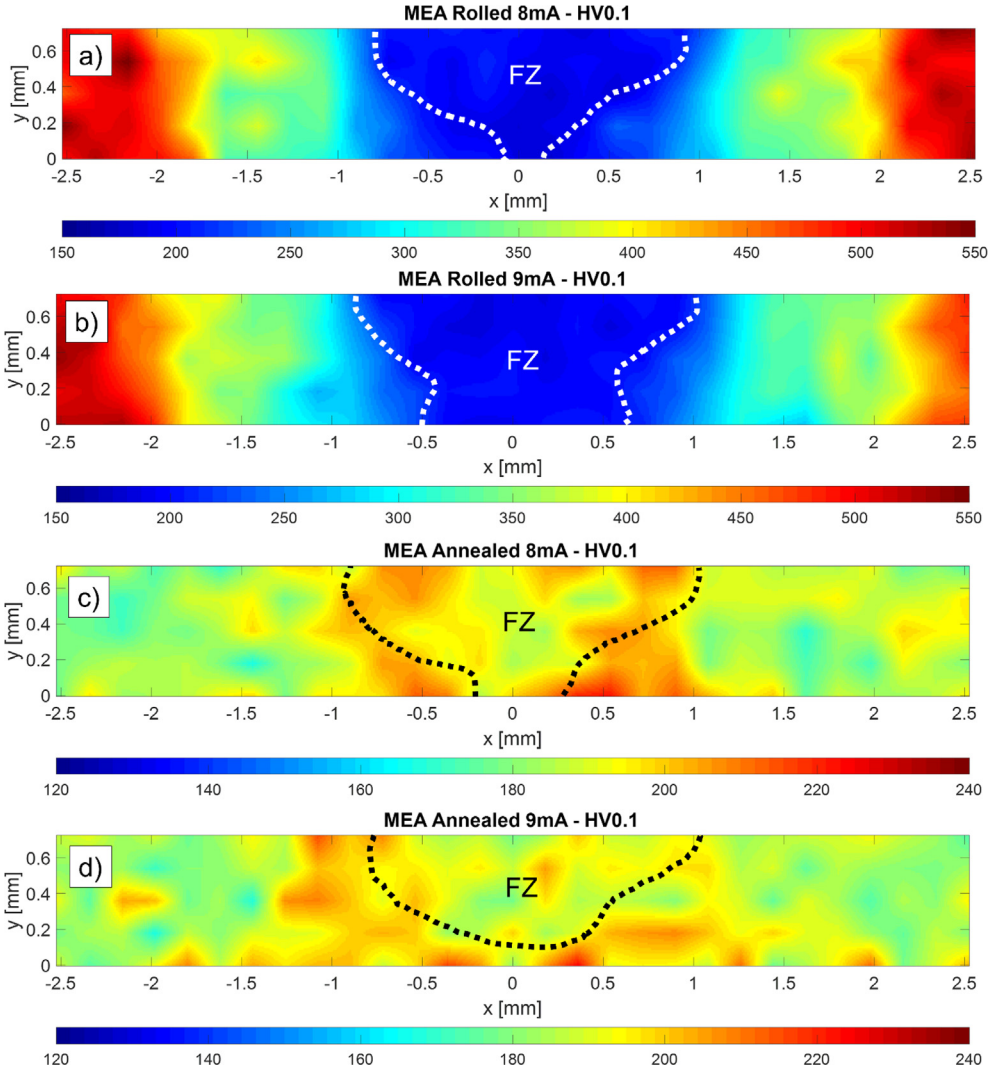

Fig. 12. Hardness maps for the MEA welds: a) cold-rolled base metal welded with 8 mA; b) cold-rolled base metal welded with 9 mA; c) annealed base metal welded with 8 mA; d) annealed base metal welded with 9 mA.

is no driving force for static recrystallisation nor sufficient time at high temperatures during welding for grain coarsening. Thus, a HAZ is considered negligible for the welds made from an initial annealed microstructure.

- It seems that the deformation texture is kept after recrystallisation for the MEA, while partially for the HEA. A mix of texture components is formed in the FZ of the MEA, while a specific ⟨100⟩ fibre along the transversal direction is formed in the FZ of the HEA.

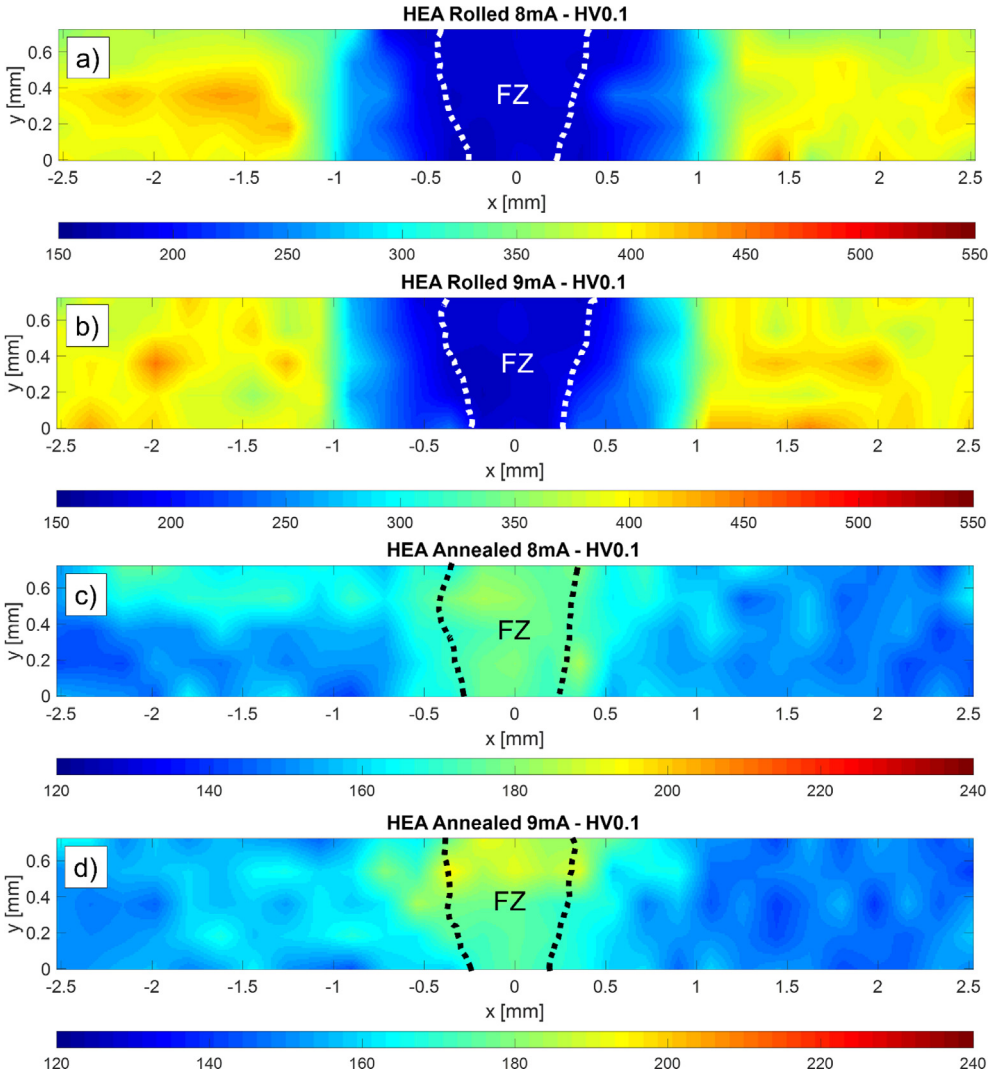

Fig. 13. Hardness maps for the HEA welds: a) cold-rolled base metal welded with 8 mA; b) cold-rolled base metal welded with 9 mA; c) annealed base metal welded with 8 mA; d) annealed base metal welded with 9 mA.

- Cobalt enriches the dendrite core, while chromium enriches the interdendritic regions of the grains in the FZ for the MEA. For the HEA, cobalt, chromium and iron enrich the dendrite core, while manganese and nickel enrich the interdendritic region of the grains in the FZ.
- The hardness values of the HAZ and FZ are smaller for the HEA welds than those of the MEA welds. The difference in the hardness in the FZ between the different conditions is negligible for a given alloy. The presence of harder zones in the FZ compared to the annealed BM for both MEA and HEA welds occur due to the formation of zone enriched with different chemical elements (microsegregation) combined with residual stresses.

Data availability

Data will be made available on request.

Declaration of Competing Interest

The authors declare that they have no known competing financial interests or personal relationships that could have appeared to influence the work reported in this paper.

Acknowledgements

We would like to thank apl.-Prof. G. Laplanche from the Technical University of Bochum, Germany, for providing the materials and Dr.-Ing. M. Schneider from the MTU Aero Engines GmbH, Germany. Ricardo Henrique Buzolin fosters the Christian Doppler Laboratory for Design of High-Performance Alloys by Thermomechanical Processing with the support of the Christian Doppler Society. Open access funding by the Graz University of Technology is also acknowledged.

Data availability

The data will be available upon request to the corresponding author.

References

[1] D.B. Miracle, O.N. Senkov, A critical review of high entropy alloys and related concepts, Acta Mater. 122 (2017) 448–511, https://doi.org/10.1016/j.actamat.2016.08.081.
[2] E.P. George, D. Raabe, R.O. Ritchie, High-entropy alloys, Nat. Rev. Mater. 4 (8) (2019) 515–534, https://doi.org/10.1038/s41578-019-0121-4.

[3] M.-H. Tsai, J.-W. Yeh, High-Entropy Alloys: A Critical Review, Mater. Res. Lett. 2 (3) (2014) 107–123, https://doi.org/10.1080/21663831.2014.912690.
[4] Y.F. Ye, Q. Wang, J. Lu, C.T. Liu, Y. Yang, High-entropy alloy: challenges and prospects, Mater. Today 19 (6) (2016) 349–362, https://doi.org/10.1016/j.mattod.2015.11.026.
[5] S. Huang et al., Mechanism of magnetic transition in FeCrCoNi-based high entropy alloys, Mater. Des. 103 (2016) 71–74, https://doi.org/10.1016/j.matdes.2016.04.053.
[6] F.D.C. Garcia Filho, R.O. Ritchie, M.A. Meyers, S.N. Monteiro, Cantor-derived medium-entropy alloys: bridging the gap between traditional metallic and high-entropy alloys, J. Mater. Res. Technol. 17 (2022) 1868–1895, https://doi.org/10.1016/j.jmrt.2022.01.118.
[7] B. Gludovatz, A. Hohenwarter, D. Catoor, E.H. Chang, E.P. George, R.O. Ritchie, A fracture-resistant high-entropy alloy for cryogenic applications, Science (80-.) 345 (6201) (2014) 1153–1158, https://doi.org/10.1126/science.1254581.
[8] N. Kumar et al., High strain-rate compressive deformation behavior of the Al0.1CrFeCoNi high entropy alloy, Mater. Des. 86 (2015) 598–602, https://doi.org/10.1016/j.matdes.2015.07.161.
[9] P. Shi et al., Enhanced strength–ductility synergy in ultrafine-grained eutectic high-entropy alloys by inheriting microstructural lamellae, Nat. Commun. 10 (1) (2019) 489, https://doi.org/10.1038/s41467-019-08460-2.
[10] N. Kumar Katiyar, K. Biswas, J.-W. Yeh, S. Sharma, C. Sekhar Tiwary, A perspective on the catalysis using the high entropy alloys, Nano Energy 88 (2021), https://doi.org/10.1016/j.nanoen.2021.106261 106261.
[11] K. Li, W. Chen, Recent progress in high-entropy alloys for catalysts: synthesis, applications, and prospects, Mater. Today Energy 20 (2021), https://doi.org/10.1016/j.mtener.2021.100638 100638.
[12] M.S. Lucas et al., Magnetic and vibrational properties of high-entropy alloys, J. Appl. Phys. 109 (7) (2011) 07E307, https://doi.org/10.1063/1.3538936.
[13] V. Chaudhary, R. Chaudhary, R. Banerjee, R.V. Ramanujan, Accelerated and conventional development of magnetic high entropy alloys, Mater. Today 49 (2021) 231–252, https://doi.org/10.1016/j.mattod.2021.03.018.
[14] P. Kumari, A.K. Gupta, R.K. Mishra, M.S. Ahmad, R.R. Shahi, A Comprehensive Review: Recent Progress on Magnetic High Entropy Alloys and Oxides, J. Magn. Magn. Mater. 554 (2022), https://doi.org/10.1016/j.jmmm.2022.169142 169142.
[15] H. Cheng et al., Review—Corrosion-Resistant High-Entropy Alloy Coatings: A Review, J. Electrochem. Soc. 168 (11) (Nov. 2021), https://doi.org/10.1149/1945-7111/ac34d0 111502.
[16] X. Zhang, N. Zhang, B. Xing, S. Yin, An Assessment of the High-Temperature Oxidation Resistance of Selected Thermal Sprayed High Entropy Alloy Coatings, J. Therm. Spray Technol. 31 (4) (2022) 1386–1403, https://doi.org/10.1007/s11666-022-01352-w.
[17] E.P. George, W.A. Curtin, C.C. Tasan, High entropy alloys: A focused review of mechanical properties and deformation mechanisms, Acta Mater. 188 (2020) 435–474, https://doi.org/10.1016/j.actamat.2019.12.015.
[18] R.K. Nutor, Q. Cao, X. Wang, S. Ding, D. Zhang, J.-Z. Jiang, Accelerated emergence of CoNi-based medium-entropy alloys with emphasis on their mechanical properties, Curr. Opin. Solid State Mater. Sci. 26 (6) (2022), https://doi.org/10.1016/j.cossms.2022.101032 101032.
[19] Z. Zhang et al., Dislocation mechanisms and 3D twin architectures generate exceptional strength-ductility-toughness combination in CrCoNi medium-entropy alloy, Nat. Commun. 8 (1) (2017) 14390, https://doi.org/10.1038/ncomms14390.
[20] Z. Li, S. Zhao, R.O. Ritchie, M.A. Meyers, Mechanical properties of high-entropy alloys with emphasis on face-centered cubic alloys, Prog. Mater. Sci. 102 (2019) 296–345, https://doi.org/10.1016/j.pmatsci.2018.12.003.
[21] M. Rhode, T. Richter, D. Schroepfer, A.M. Manzoni, M. Schneider, G. Laplanche, Welding of high-entropy alloys and compositionally complex alloys—an overview, Weld. World 65 (8) (2021) 1645–1659, https://doi.org/10.1007/s40194-021-01110-6.
[22] M. Nahmany, Z. Hooper, A. Stern, V. Geanta, I. Voiculescu, AlxCrFeCoNi High-Entropy Alloys: Surface Modification by Electron Beam Bead-on-Plate Melting, Metallogr. Microstruct. Anal. 5 (3) (2016) 229–240, https://doi.org/10.1007/s13632-016-0276-y.
[23] R. Sokkalingam, P. Mastanaiah, V. Muthupandi, K. Sivaprasad, K.G. Prashanth, Electron-beam welding of high-entropy alloy and stainless steel: microstructure and mechanical properties, Mater. Manuf. Process. 35 (16) (2020) 1885–1894, https://doi.org/10.1080/10426914.2020.1802045.
[24] Z. Wu, S.A. David, Z. Feng, H. Bei, Weldability of a high entropy CrMnFeCoNi alloy, Scr. Mater. 124 (2016) 81–85, https://doi.org/10.1016/j.scriptamat.2016.06.046.
[25] M. Schneider et al., Analysis of strengthening due to grain boundaries and annealing twin boundaries in the CrCoNi medium-entropy alloy, Int. J. Plast. 124 (2020) 155–169, https://doi.org/10.1016/j.ijplas.2019.08.009.
[26] G. Laplanche, A. Kostka, C. Reinhart, J. Hunfeld, G. Eggeler, E.P. George, Reasons for the superior mechanical properties of medium-entropy CrCoNi compared to high-entropy CrMnFeCoNi, Acta Mater. 128 (2017) 292–303, https://doi.org/10.1016/j.actamat.2017.02.036.
[27] C. Stephan-Scherb, W. Schulz, M. Schneider, S. Karafiludis, G. Laplanche, High-Temperature Oxidation in Dry and Humid Atmospheres of the Equiatomic CrMnFeCoNi and CrCoNi High- and Medium-Entropy Alloys, Oxid. Met. 95 (1) (2021) 105–133, https://doi.org/10.1007/s11085-020-10014-7.
[28] Y. Mei et al., Effect of base metal and welding speed on fusion zone microstructure and HAZ hot-cracking of electron-beam welded Inconel 718, Mater. Des. 89 (2016) 964–977, https://doi.org/10.1016/j.matdes.2015.10.082.
[29] M. Orłowska, F. Pixner, K. Majchrowicz, N. Enzinger, L. Olejnik, M. Lewandowska, Application of Electron Beam Welding Technique for Joining Ultrafine-Grained Aluminum Plates, Metall. Mater. Trans. A 53 (1) (2022) 18–24, https://doi.org/10.1007/s11661-021-06509-w.
[30] K. Easterling, "Chapter3 - The heat-affected zone," in: Introduction to the Physical Metallurgy of Welding (Second Edition), Second Edi., K. Easterling, Ed. Butterworth-Heinemann, 1992, pp. 126–190. doi: https://doi.org/10.1016/B978-0-7506-0394-2.50008-3.
[31] D.N. Lee, The evolution of recrystallization textures from deformation textures, Scr. Metall. Mater. 32 (10) (1995) 1689–1694, https://doi.org/10.1016/0956-716X(95)00256-U.
[32] Y. Zhou, J.J. Jonas, J. Savoie, A. Makinde, S.R. MacEwen, Effect of texture on earing in FCC metals: Finite element simulations, Int. J. Plast. 14 (1) (1998) 117–138, https://doi.org/10.1016/S0749-6419(97)00044-2.
[33] M. Ahmad, J.I. Akhter, M. Akhtar, M. Iqbal, E. Ahmed, M.A. Choudhry, Microstructure and hardness studies of the electron beam welded zone of Hastelloy C-276, J. Alloys Compd. 390 (1) (2005) 88–93, https://doi.org/10.1016/j.jallcom.2004.08.031.
[34] M.S. Węglowski, S. Błacha, A. Phillips, Electron beam welding – Techniques and trends – Review, Vacuum 130 (2016) 72–92, https://doi.org/10.1016/j.vacuum.2016.05.004.
[35] K. Easterling, "Chapter2 - The weld metal," in: Introduction to the Physical Metallurgy of Welding (Second Edition), Second Edi., K. Easterling, Ed. Butterworth-Heinemann, 1992, pp. 55–125. doi: https://doi.org/10.1016/B978-0-7506-0394-2.50007-1.
[36] K. Jin et al., Tailoring the physical properties of Ni-based single-phase equiatomic alloys by modifying the chemical complexity, Sci. Rep. 6 (1) (2016) 20159, https://doi.org/10.1038/srep20159.
[37] G. Laplanche, P. Gadaud, O. Horst, F. Otto, G. Eggeler, E.P. George, Temperature dependencies of the elastic moduli and thermal expansion coefficient of an equiatomic, single-phase CoCrFeMnNi high-entropy alloy, J. Alloys Compd. 623 (2015) 348–353, https://doi.org/10.1016/j.jallcom.2014.11.061.
[38] G. Laplanche et al., Elastic moduli and thermal expansion coefficients of medium-entropy subsystems of the CrMnFeCoNi high-entropy alloy, J. Alloys Compd. 746 (2018) 244–255, https://doi.org/10.1016/j.jallcom.2018.02.251.
[39] C. Donadille, R. Valle, P. Dervin, R. Penelle, Development of texture and microstructure during cold-rolling and annealing of F.C.C. alloys: Example of an austenitic stainless steel, Acta Metall. 37 (6) (1989) 1547–1571, https://doi.org/10.1016/0001-6160(89)90123-5.
[40] K.B. Tazuddin, N.P. Gurao, Deciphering micro-mechanisms of plastic deformation in a novel single phase fcc-based MnFeCoNiCu high entropy alloy using crystallographic texture, Mater. Sci. Eng. A 657 (2016) 224–233, https://doi.org/10.1016/j.msea.2016.01.065.
[41] X.W. Liu et al., Columnar to equiaxed transition and grain refinement of cast CrCoNi medium-entropy alloy by microalloying with titanium and carbon, J. Alloys Compd. 775 (2019) 1068–1076, https://doi.org/10.1016/j.jallcom.2018.10.187.
[42] Z. Wu, S.A. David, D.N. Leonard, Z. Feng, H. Bei, Microstructures and mechanical properties of a welded CoCrFeMnNi high-entropy alloy, Sci. Technol. Weld. Join. 23 (7) (Oct. 2018) 585–595, https://doi.org/10.1080/13621718.2018.1430114.
[43] B. Cantor, I.T.H. Chang, P. Knight, A.J.B. Vincent, Microstructural development in equiatomic multicomponent alloys, Mater. Sci. Eng. A 375–377 (2004) 213–218, https://doi.org/10.1016/j.msea.2003.10.257.
[44] G.A. Salishchev et al., Effect of Mn and V on structure and mechanical properties of high-entropy alloys based on CoCrFeNi system, J. Alloys Compd. 591 (2014) 11–21, https://doi.org/10.1016/j.jallcom.2013.12.210.
[45] M. Laurent-Brocq et al., Insights into the phase diagram of the CrMnFeCoNi high entropy alloy, Acta Mater. 88 (2015) 355–365, https://doi.org/10.1016/j.actamat.2015.01.068.